

ARTICLE OPEN

Characterization of corrosion resistance of C/C–SiC composite in molten chloride mixture MgCl₂/NaCl/KCl at 700 °CWenjin Ding¹, Yuan Shi^{2*}, Fiona Kessel², Dietmar Koch² and Thomas Bauer³

Due to their high thermal stability and low cost, molten chlorides are promising high-temperature fluids for example for thermal energy storage (TES) and heat transfer fluid (HTF) materials in concentrated solar power (CSP) plants and other applications. However, the commercial application of molten chlorides is strongly limited due to their strong corrosivity against commercial alloys at high temperatures. The work addresses on a fundamental level whether carbon based composite ceramics could be potentially utilized for some corrosion critical components. Liquid silicon infiltration (LSI) based carbon fiber reinforced silicon carbide (called C/C–SiC) composite is immersed in a molten chloride salt (MgCl₂/NaCl/KCl 60/20/20 mole%) at 700 °C for 500 h under argon atmosphere. The material properties and microstructure of the C/C–SiC composite with and without exposure in the molten chloride salt have been investigated through mechanical testing and analysis with scanning electron microscopy (SEM) and energy-dispersive X-ray (EDX) scanning. The results reveal that the C/C–SiC composite maintains its mechanical properties after exposure in the strongly corrosive molten chloride salt. The oxidizing impurities in the molten salt react only with residual elemental silicon (Si) in the area of the C/C–SiC matrix. In comparison, no indication of reaction between the molten chloride salt and carbon fiber or SiC in the matrix is observed. In conclusion, the investigated C/C–SiC composite has a sound application potential as a structural material for high-temperature TES and HTF with molten chlorides due to its excellent corrosion resistance and favorable mechanical properties at high temperatures.

npj Materials Degradation (2019)3:42; <https://doi.org/10.1038/s41529-019-0104-3>

INTRODUCTION

As an emerging renewable energy technology, the global capacity of installed concentrated solar power (CSP) plants has a significant increase from ~0.3 to 4.8 GW from 2005 to 2015, in particular from 2010 to 2015 grew at an average rate of 50% per year.¹ In the state-of-the-art commercial CSP plants, the heat from sunlight is stored and transferred in thermal energy storage (TES) and heat transfer fluid (HTF) materials such as molten salts (e.g., Solar Salt: NaNO₃/KNO₃ 60/40 wt.%, a typical commercial TES/HTF material), which allows them to generate dispatchable and low-cost power during the absence of sunlight.² The properties of commonly considered molten salts as TES materials in CSP are compared in Table 1. Due to the thermal decomposition at above ~550 °C, the operating temperature of the commercial nitrate/nitrite salts is limited.

Compared with the commercial molten nitrate/nitrite salts, molten chloride salts not only have high thermal stability (stable at >800 °C), but also lower costs (see Table). These advantages could lead to a reduced levelized cost of electricity (LCOE) of CSP. The high thermal stability allows to operate them at higher temperatures for higher efficiency of thermal to electrical energy conversion for CSP.³ Thus, over the course of the SunShot Initiative, the U.S. Department of Energy (DOE) identified the development of molten chloride salts as one major option for next generation CSP plants (Gen-3 CSP).⁴

However, molten chlorides are strongly corrosive to metallic structural materials at high temperatures, which is a main challenge for their application in next generation CSP plants.^{3–8} Table 2 shows the corrosion rates (CRs) of commercial Fe–Ni–Cr alloys in the Solar Salt and various molten chloride salts under different conditions (e.g., temperatures and atmospheres).^{5,7–10} It

reveals that even under inert atmosphere the Ni-based superalloys like Hastelloy X or C-276 (cost > \$20 per kg) in molten chlorides (e.g., MgCl₂/NaCl/KCl at 700 °C⁹) have the CRs much higher than the required CR in commercial applications (<10 μm/year for 30 year's lifetime.⁹) Besides the corrosion resistance, the mechanical strength of alloys decreases with increasing temperature, particularly at >600 °C (named Creep Cliff, e.g., the allowable stress of Hastelloy N for 100,000 h decreases significantly from ~80 to ~25 MPa with increasing temperature from 600 to 700 °C.¹¹ One approach is adding a corrosion inhibitor (e.g., Mg metal) in the molten chloride salts to reduce metallic CRs.¹² In the present paper, we focus on carbon fiber reinforced silicon carbide (C/C–SiC) composite as an alternative structural material for corrosion critical components in chloride molten salt systems.

Owing to the excellent mechanical properties, fracture toughness and corrosion resistance, carbon fiber reinforced silicon carbide (C/C–SiC) composite is a potentially attractive high-temperature structural material for energy-related applications. For instance, it could be potentially used in corrosion critical components, such as pumps and valves for CSP plants and molten salt nuclear power plants.^{13–15} However, to our best knowledge, there is a lack of studies on its corrosion resistance of the C/C–SiC composite to strongly corrosive molten chlorides at high temperatures (>600 °C), which contain corrosive impurities (e.g., hydroxide species) due to hydrolysis of the hydrated water in the chloride salts.⁹

In this work, the C/C–SiC composite, which was developed via liquid silicon infiltration (LSI) at the Institute of Structures and Design of German Aerospace Center (DLR), is immersed in a molten chloride mixture (MgCl₂/NaCl/KCl 60/20/20 mole%) at 700 °C for 500 h under argon atmosphere. The material properties

¹Institute of Engineering Thermodynamics, German Aerospace Center (DLR), Stuttgart, Germany. ²Institute of Structures and Design, German Aerospace Center (DLR), Stuttgart, Germany. ³Institute of Engineering Thermodynamics, German Aerospace Center (DLR), Cologne, Germany. *email: yuan.shi@dlr.de

Table 1. Properties of commonly used molten salts as TES materials in CSP.⁹

Molten salts composition (wt.%)	Melting point (°C)	Stability limit (°C)	Heat capacity (kJ kg ⁻¹ K ⁻¹)	Cost (\$/kg)
Solar Salt NaNO ₃ /KNO ₃ (60/40)	240 ²²	530–565 ²²	1.55 (500 °C) ²²	~1 ²²
Hitec NaNO ₃ /KNO ₃ / NaNO ₂ (7/53/40)	142 ¹⁰	535 ¹⁰	1.56 (300 °C) ¹⁰	0.7–1.1 ¹⁰
MgNaK chlorides MgCl ₂ /NaCl/KCl (68.2/14.0/17.8)	380 ²	>800 ²³	~1.0 (500~800 °C) ²³	<0.5 ⁹

Table 2. Corrosion of Fe-Ni-Cr-based alloys in commonly used molten salts as TES materials.

Molten salts	Alloys	Ni (wt.%)	T (°C)	Corrosion rate (µm/year)
Solar Salt	SS 316	10–14	600	16 _a ¹⁰
ZnNaK chlorides	SS 304	8–11	400	>15 _b ⁵
ZnCl ₂ /NaCl/KCl (68.6/ 7.5/23.9 wt.%)	Ha C-22	~56	400	~ 8 _b ⁵
	Ha C-22	~56	800	~ 12 _b ⁵
	Ha C-276	~57	800	~ 5 _b ⁵
MgNaCa chlorides MgCl ₂ /NaCl/CaCl ₂ (14.95/53.43/ 31.61 mole%)	IN 625	~62	600	121 _a ⁷
	Ha X	~47	600	153 _a ⁷
NaLi chlorides NaCl/LiCl (34.42/ 65.58 wt.%)	Ha B-3	~65	600	145 _a ⁷
	SS 347	9–12	650	7490 _b ⁸
	SS 310	~20.5	650	6420 _b ⁸
MgNaK chlorides MgCl ₂ /NaCl/KCl (60/20/ 20 mole%)	In 800 H	30–35	650	5940 _b ⁸
	IN 625	~62	650	2800 _b ⁸
	SS 310	19–22	700	1752 _b ⁹
	In 800 H	30–35	700	876 _b ⁹
	Ha C-276	~57	700	526 _b ⁹

SS Stainless steel, Ha Hastelloy, IN Inconel, In Incoloy, a in air, b in inert atmosphere

and microstructures of the C/C–SiC composite before and after exposure in the molten chloride salt are investigated through different mechanical tests and analysis with scanning electron microscopy (SEM) and energy-dispersive X-ray (EDX). Moreover, the corrosion mechanism of the C/C–SiC composite in the molten chloride salt is discussed based on the microstructural analysis.

RESULTS AND DISCUSSION

Mechanical properties

The measured interlaminar shear strength (ILSS_C), 3PB-strength (σ_{3PB}), Young's modulus (*E*) and strain of failure (ε_{3PB}) are summarized in Table 3. Samples with and without exposure to the molten chloride salt at 700 °C are compared. The table shows average values of three measurements with the standard deviation.

The ILSS_C value of the C–SiC composite is a matrix dominated property and the values of the coupons with and without exposure in the molten chloride salt are nearly identical. Therefore, no influence of exposure in the molten chloride salt for 500 h at 700 °C on the properties of matrix (C–SiC) can be identified. The results of 3PB tests with consideration of the standard deviation (summarized in Table) show that the values of strength (σ_{3PB}) and

Table 3. Summary of results from mechanical tests.

Exposure in molten salt	ILSS _C (MPa)	σ _{3PB} (MPa)	<i>E</i> (GPa)	ε _{3PB} (%)
No	27.8 ± 1.7	156.7 ± 5.6	64.2 ± 0.9	0.41 ± 0.05
Yes	27.9 ± 3.4	153.2 ± 7.7	58.6 ± 1.3	0.40 ± 0.03

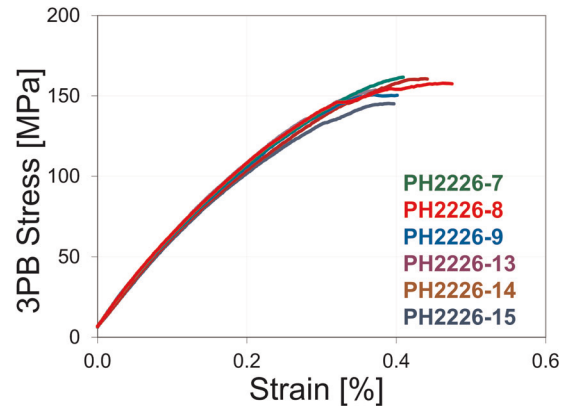


Fig. 1 Stress–strain curves of 3PB tests for the coupons without exposure (PH2226-7 to -9) and with exposure (PH2226-13 to -15).

fracture strain (ε_{3PB}) from the coupons with and without exposure are almost same. The measured Young's modulus (*E*) shows ~9% difference after the exposure, which will be explained with the microstructural analysis results in section "Analysis" of microstructure for corrosion mechanisms. The stress–strain response in Fig. 1 shows a quasi-ductile behavior for all the coupons before and after exposure. Moreover, no significant influence of exposure in the molten chloride salt on the bending properties of C/C–SiC materials can be determined. This shows strong agreement with the measured values in Table 3.

Analysis of microstructure for corrosion mechanisms

In this section, the microstructure of three different C/C–SiC sample sections (for more details see Fig. 12 in section Microstructural analysis) with and without salt exposure was evaluated by SEM and EDX analysis.

Analysis of surface A. First, surface A (front surface of C/C–SiC sample body in Fig. 12) of the sample without salt exposure shows the "block formation" (see Fig. 2a), which is typical for C/C–SiC material:¹⁶ carbon fiber bundle forms block-like parts which are separated and encapsulated by Si and SiC veins (Fig. 2a). Figure 2b shows the front surface of C/C–SiC sample after exposure in the molten chloride salt for 500 h at 700 °C. The surface was cleaned in an ultrasonic bath before image acquisition. In comparison with Fig. 2a, the analysis of the exposed samples shows that the microstructure does not undergo major changes after exposure (Fig. 2b). However, despite cleaning through ultrasonic cleaning bath some salt residues remain on the surface of the exposed C/C–SiC sample.

In order to evaluate the impact of salt exposure, the elemental composition of surface A of C/C–SiC samples before and after exposure was determined via EDX. As expected, the untreated samples contained carbon and silicon exclusively (Fig. 3), while no components of the chloride salt can be found on the sample.

In comparison with the C/C–SiC sample without exposure, elements from the molten salt (Mg, Na, K, Cl) are detected on surface A of the C/C–SiC material after exposure (Fig. 4). In addition, the analysis shows oxygen element. It is concluded that

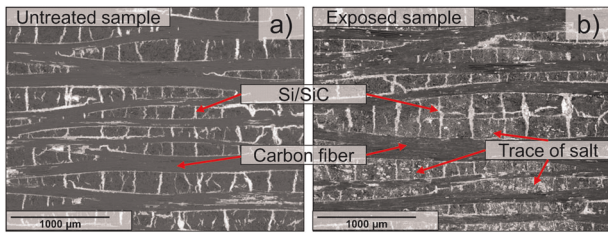


Fig. 2 SEM images of surface A (front surface) of C/C-SiC samples: (a) without exposure and (b) with exposure.

oxygen comes from the impurities in the molten salt, e.g., MgOH^+ . It is imperative for a correct evaluation of corrosion to distinguish between real corrosion products (salt reacts with substrate) and residues (salt components deposit mechanically on substrate) remaining on the C/C-SiC sample surface (Fig. 2b). The reaction of a salt component with carbon can be excluded as there is no significant overlay between the carbon element and the salt elements. Also, the glass carbon crucible used in this work shows no reaction with the salt. This is different however in regard to the Si, Mg, and O elements. A significant congruence in the area of the silicon veins can be seen between these elements (Fig. 4). This reveals that the Si components (Si or SiC) could react with the

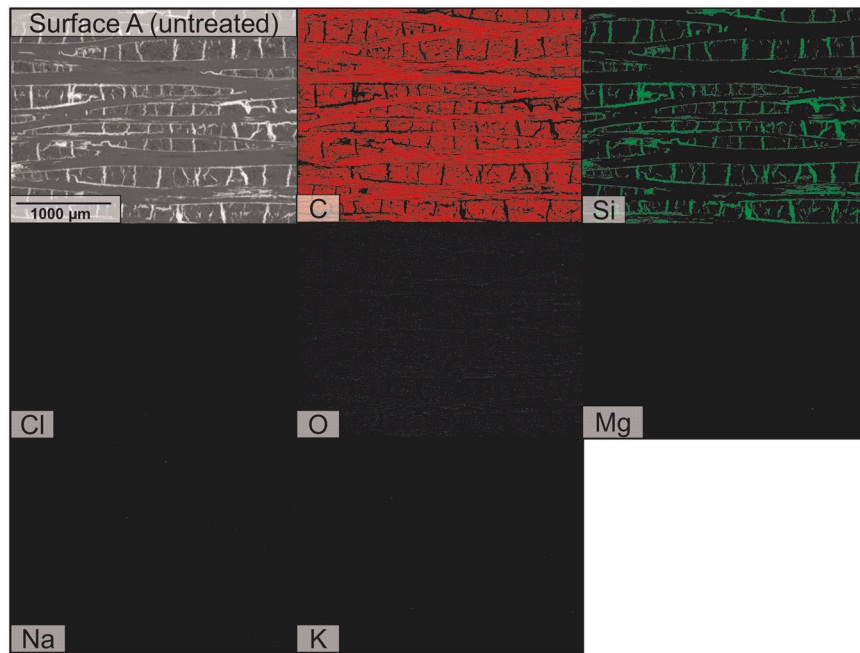


Fig. 3 EDX Analysis of surface A (front surface) without exposure in the molten salt.

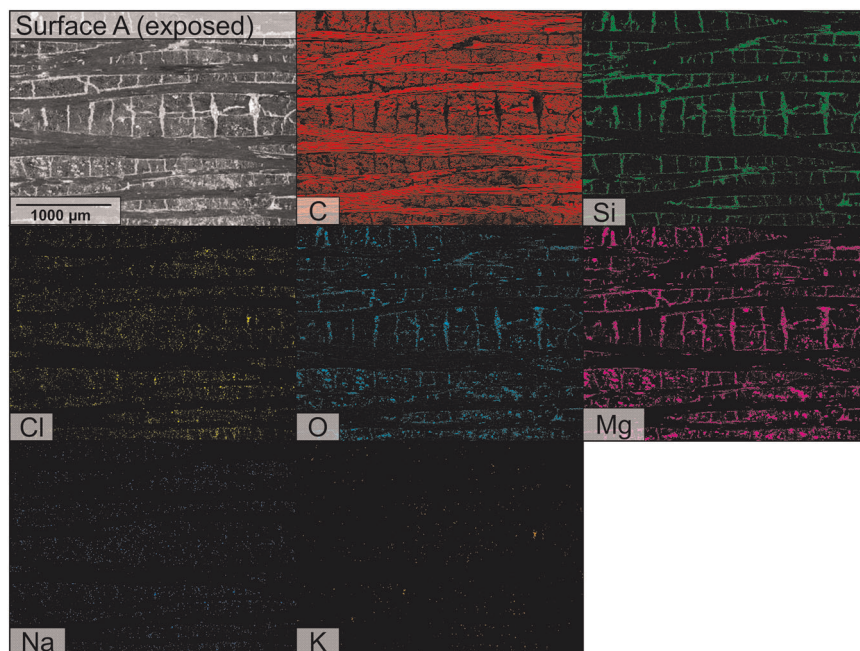


Fig. 4 EDX-Analysis of surface A (front surface) with exposure in the molten salt.

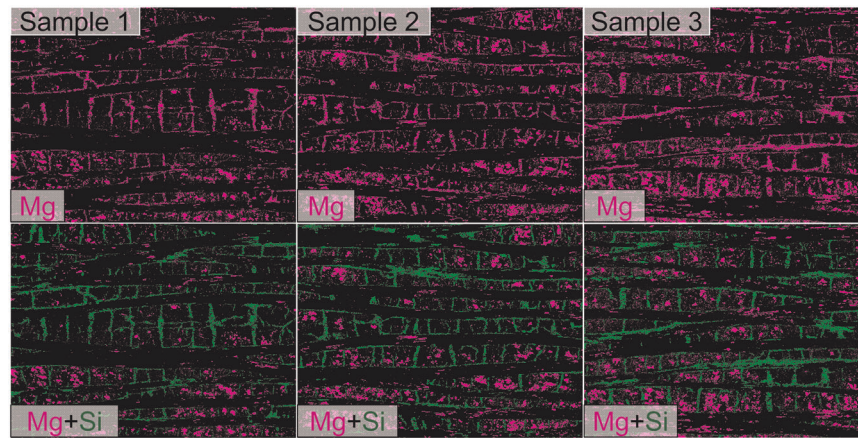


Fig. 5 Overlapping of Mg and Si elements detected by EDX-Analysis on surface A (front surface) of three exposed samples.

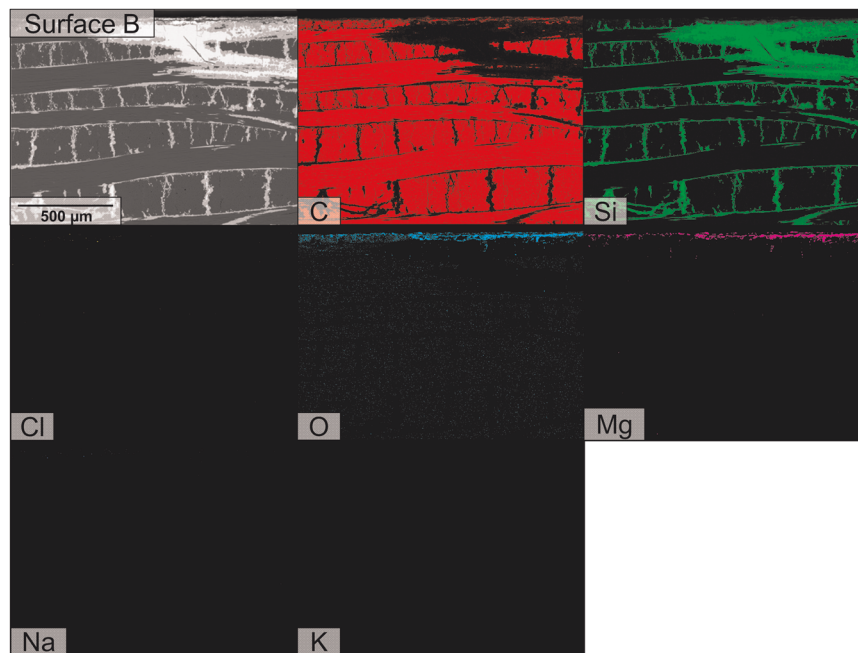


Fig. 6 EDX-Analysis of the exposed surface B "in plane" (cross section).

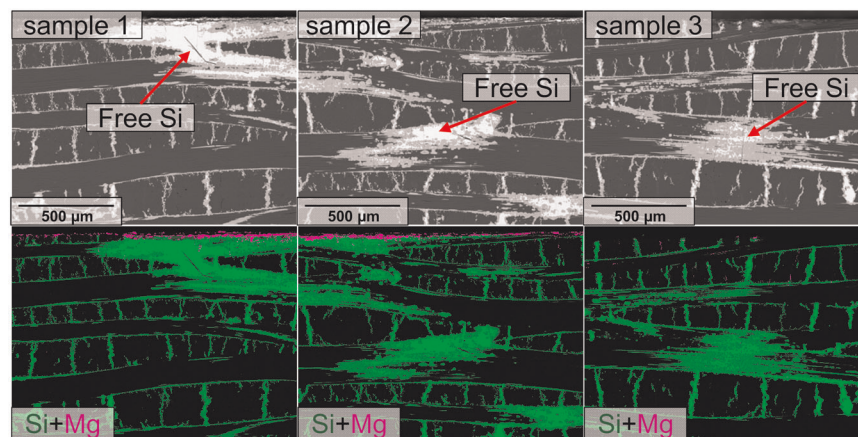


Fig. 7 Overlapping of Mg and Si elements detected by EDX-analysis on surface B "in plane" (cross section) of three exposed samples.

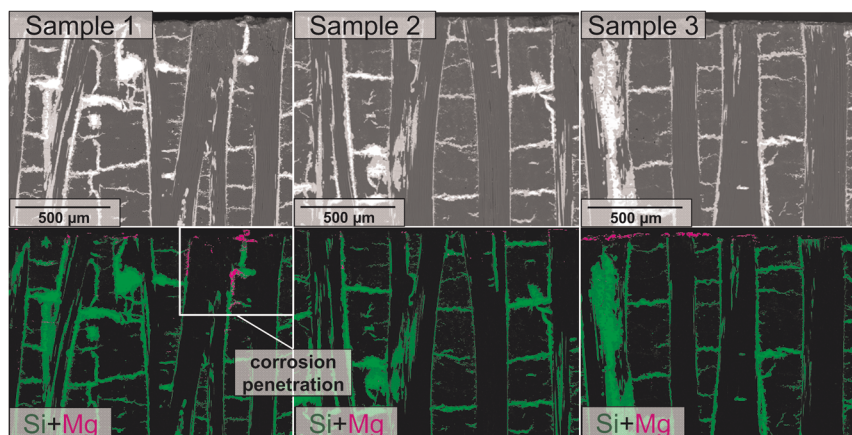
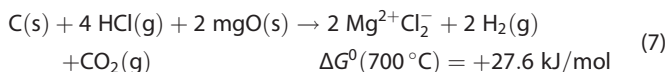
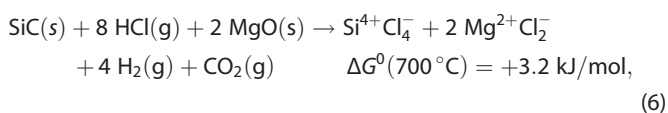
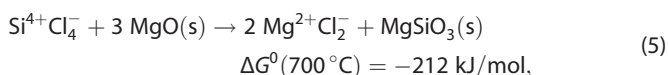
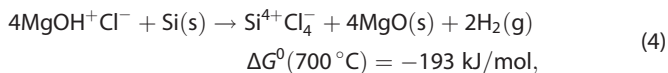
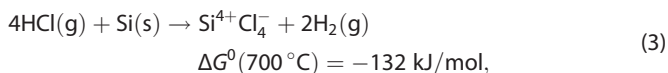


Fig. 8 Overlapping of Mg and Si elements detected by EDX-analysis on surface B, “perpendicular” (cross section) of three exposed samples.

molten chloride salt. In order to cleanly demonstrate the reaction of the Si components (Si or SiC) with the molten chloride salt during the exposure, an extended analysis via overlapping the salt element (e.g., Mg, O) and Si EDX-images (see Fig. 5 for Mg and Si) shows in more detail that silicon veins overlap with the signal of the salt element (here Mg). The visible Mg on the overlay image (Fig. 5 lower panel) indicates that salt residues in form of MgO or MgCl₂ also remain on the surface, trapped by the rough sample surface similar to the other residues such as NaCl and KCl.

In our previous work,⁹ it has been found that the impurities MgOH⁺ and H⁺ in the molten chloride salt, which are produced due to hydrolysis of the hydrated salts (e.g., hydrated MgCl₂) during the heating as shown in Eqs. 1–2, could react with the Si element in the commercial alloy SS 310 (containing ~2% Si) to form some Mg–Si oxides (e.g., MgSiO₃) at 700 °C (see Eqs. 3–5). The thermodynamic calculations using the commercial software—FactSage® show that the standard Gibbs free energy of the reactions in Eqs. 3–5 at 700 °C is –132, –193, and –212 kJ/mol, respectively, whereas the reaction of HCl with SiC and C (Eqs. 6–7) has the standard Gibbs free energy of +3.2 and +27.6 kJ/mol, respectively. This means that only free Si can react with the corrosive impurities in the molten salt at 700 °C.



Analysis of surface B. The second part of the microstructure evaluation is to investigate the C/C–SiC sample cross sections after the salt exposure: surface B in Fig. 12b. The images are similar to

the previous experiments showing the mapping of the elements in the molten salt (Fig. 6). Since the material consists of C and Si, these elements dominate the mapping result. As previously seen in Fig. 2b and Fig. 4 there are salt and Mg–O–Si deposits detected on the surface of the sample, but none within the sample (Fig. 6).

To get a better understanding of the corrosion penetration, representative images of the samples are again compared via superimposition of Mg onto Si (Fig. 7). In contrast to Fig. 5, the dominant signal comes from Si. This indicates the extent to which corrosion (visible as Mg) penetrates the material. In particular sample 1 of Fig. 7 shows that, despite the big amount of free silicon (white area in SEM image), no deep corrosion has occurred inside the material. This becomes especially clear when almost no silicon is present at the surface (sample 3 of Fig. 7), as in this case no corrosion products can be detected at all.

Following the “in plane” view of surface B (Fig. 7), the penetration behavior of salt perpendicular to the fabric layers (Fig. 12b) was investigated and Fig. 8 shows the results with overlay of silicon and magnesium. Similar to the result of “in plane” in Fig. 7, samples generally show no penetration of corrosion into the material, neither in the area of the Si/SiC veins nor in the C/C blocks. Only sporadically ‘corrosion’ enters the material (sample 1 of Fig. 8). Since this is not a common case, the question arises what might be responsible for this occurrence of corrosion in those rare cases.

One assumption that has not yet been further investigated is that the porosity of the C/C–SiC material is responsible for this. C/C–SiC usually has an open porosity between 1 and 3%¹⁷ (in our case approximately 2.3%). Thus, there is a certain amount of cavities in the material which can allow the molten salt to penetrate into the material. Especially in the case of pores or cracks through SiC areas and alongside free silicon, corrosion could occur directly inside the material by reacting with free Si. Figure 9 shows an example of a pore of an untreated material on which the described effect could occur.

A further analysis of the corrosion mechanisms between the molten salt and C/C–SiC material was conducted through sample 1 from exposed surface B, “perpendicular” (Fig. 8) with enlargement area and the results are shown in Fig. 10. The associated mappings in Fig. 10c and d show in which specific areas of the silicon veins corrosion takes place. Clear border between SiC and molten salt can be observed. This indicates that the SiC in the matrix of C/C–SiC material did not react with molten salt at 700 °C and for 500 h. This is also confirmed by the thermodynamic calculation (Eqs. 6–7). Furthermore, practically unchanged mechanical properties with and without molten chloride salt exposure also confirm that the matrix of C/C–SiC material was not attacked. On the other hand, the vague interfaces of Mg and O in the free Si area show the ongoing corrosion reaction in Fig. 10 c, d.

Furthermore, it should be noticed that free Si area remained after the exposure test, which can be explained through three ways:

- Because of the limited exposure time (500 h) the corrosion reaction were interrupted;
- A lack of the corrosive impurities in the molten salt system due to the consumption by corrosion may significantly retard the CR;
- Due to the fact that the free silicon is usually isolated by the SiC and SiC shows strong resistance to the molten salt, the corrosion is mainly located and strongly limited for the investigated C/C–SiC composite.

The corrosion resistance of C/C–SiC composites against the molten chloride salt ($\text{MgCl}_2/\text{NaCl}/\text{KCl}$ 60/20/20 mole%) was investigated at 700 °C for 500 h under argon atmosphere by testing their mechanical properties and analyzing their microstructures with SEM and EDX after exposure.

The main conclusions of this work are:

- The excellent mechanical properties of the C/C–SiC material (interlaminar shear strength, 3PB-strength, Young's modulus and strain of failure) were kept after exposure in the strongly corrosive molten chlorides.

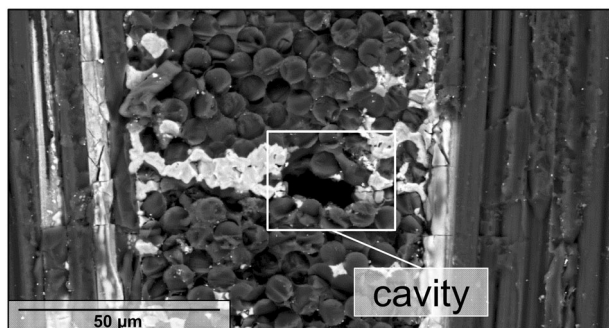


Fig. 9 Close-up of the sample surface of a C/C–SiC material, with a cavity alongside a Si–SiC vein.

- The SEM and EDX results show that oxidizing impurities in the molten salt react with residual elemental silicon. The corrosion products could be Mg–Si oxides. In comparison, the C and SiC components in the material don't react with the molten salt. This explains that exposure in the molten chloride salt does not influence the mechanical properties of the C/C–SiC material.
- Most of the corrosion products are found on the surface of the C/C–SiC material. The corrosion only occasionally penetrates into the interior of the C/C–SiC material in areas of the Si/SiC veins with the pores or cracks through SiC areas and alongside free silicon. This reveals the pores (i.e., porosity) in the C/C–SiC material have significant effect on its corrosion resistance.
- No direct analogy to the corrosion effects of alloys can be drawn for the C/C–SiC composite, since corrosion in the alloys generally causes an even and flat spread into the material interior. The corrosion pattern of C/C–SiC does not show this effect due to the heterogeneous composition of the material (fiber-matrix composition). Furthermore the data indicates that corrosion occurs only on very limited spots in the material and exclusively on residual free silicon. For this reason, no CR was stated.
- Due to its excellent corrosion resistance and favorable mechanical properties at high temperatures, the C/C–SiC composite has a sound application potential as a structural material for high-temperature TES and HTF with molten chlorides.

For a comparison with our previous work for corrosion of commercial alloys, the same $\text{MgCl}_2/\text{NaCl}/\text{KCl}$ (60/20/20 mole%) salt mixture and corrosion test conditions were used in this work. In our future work, the eutectic salt from literature¹⁸ or our ongoing work will be used for corrosion tests in a more real condition.

METHODS

C/C–SiC composite

In this work, C/C–SiC composite samples were manufactured via Liquid Silicon Infiltrated (LSI) process at the Institute of Structures and Design of German Aerospace Center (DLR). The manufacturing process can be

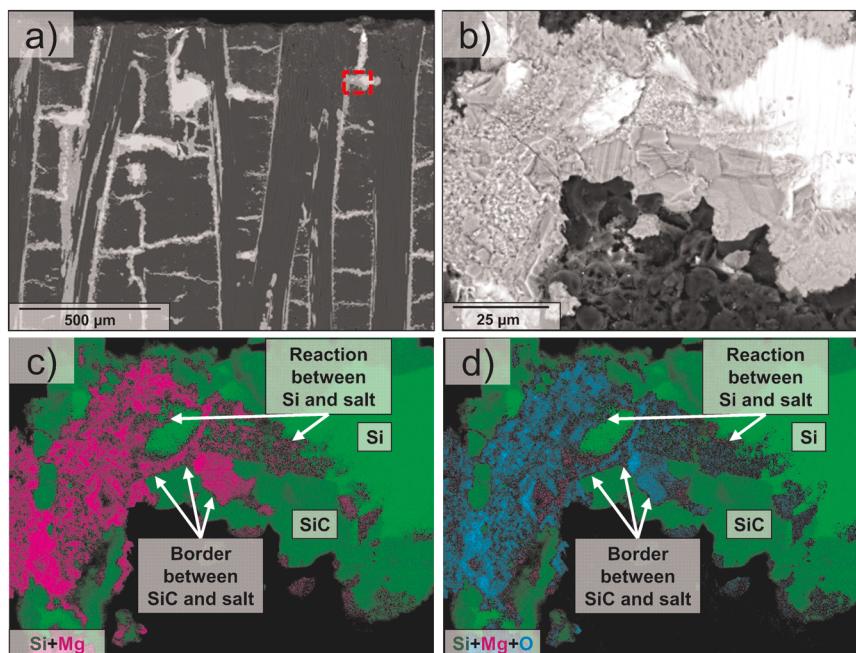
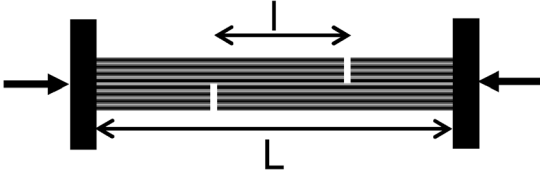



Fig. 10 SEM images of the sample 1 (Fig. 8) for exposed surface B “perpendicular” (cross section). **a** Virgin size. **b** enlargement of dash-lined region in (a); EDX-analysis with the overlay of the Mg-, Si-channels and **(d)** EDX-analysis with the overlay of the Mg-, O- and Si-channels.

Table 4. Specimen geometry, loading direction and test dimension.

Test Type	Specimen geometry and loading direction	Test dimension	Tested mechanical properties
Compression-shear (DIN EN 658-4)		$L = 20 \text{ mm}$ and $l = 8 \text{ mm}$	Interlaminar shear strength (ILSS _c)
Three-point-bending (DIN EN 658-3)		$L/t = 20$ and $t = 2.3 \text{ mm}$	3PB-strength (σ_{3PB}), Young's modulus (E) and strain of failure (ϵ_{3PB})

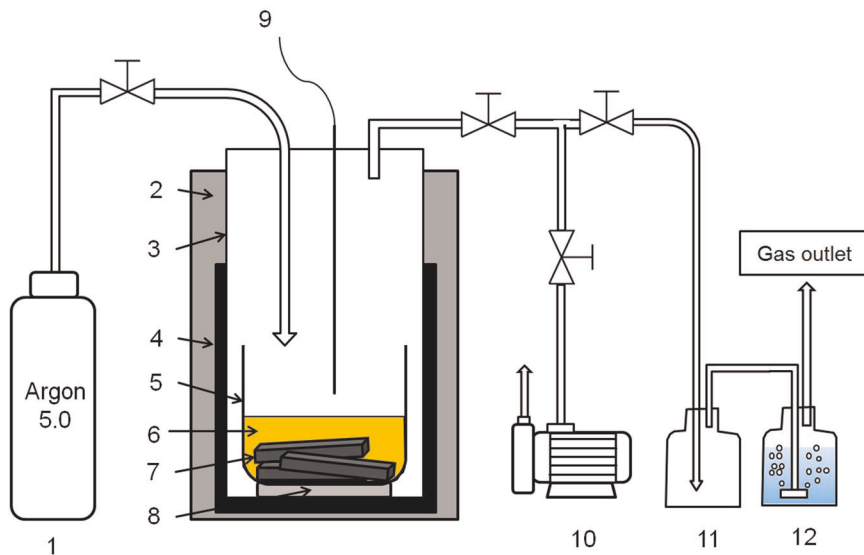


Fig. 11 Schematic diagram of experimental set-up for immersion tests in molten $\text{MgCl}_2/\text{KCl}/\text{NaCl}$. 1: Gas bottle for argon 5.0 gas, 2: Glass wool heat isolator, 3: Steel tubing of Incoloy 800 H, 4: Furnace, 5: Glassy carbon crucible, 6: Molten chloride salt, 7: coupons of the C/C-SiC composite, 8: Al_2O_3 plate, 9: Thermocouple close to the molten salt, 10: Vacuum pump, 11: Security bottle (empty) to prevent reflux from the gas washing bottle, 12: Bottle with NaOH solution for gas washing (removal of HCl and Cl_2).

subdivided in three main stages. First, CFRP (Carbon Fiber Reinforced Polymers) preforms were produced using a resin preimpregnated fabric (prepreg), based on phenolic resin precursor and a 2D carbon fiber fabric as raw material. The prepreg layup was densified and cured by warm pressing ($T_{\text{max}} = 240^\circ\text{C}$, $P_{\text{max}} = 5.8 \text{ kPa}$). In the second step, the CFRP preform was pyrolyzed at a temperature above 900°C in N_2 atmosphere at ambient pressure. In this step the polymer matrix was transformed to a carbon matrix, resulting in a porous C/C preform. Finally, the C/C structure was siliconized at $T_{\text{max}} = 1650^\circ\text{C}$ in vacuum ($<2 \text{ mbar}$). SiC matrix was built up by a chemical reaction of Si and C at the contact surfaces of the microcracks, leading to a dense C/C-SiC material, which is characterized by load bearing carbon fiber bundles embedded in a SiC matrix with a small amount of residual Si and C. The fiber volume content (FVC) and porosity of the investigated plates are approximately 57.0% and 2.3%, respectively. The coupons for the compression-shear and three-points-bending (3PB) tests were cut from a composite plate (approximately $80 \text{ mm} \times 80 \text{ mm}$ with thickness of 2.3 mm) using diamond saw. The geometry of bending samples is listed in Table 4.

Corrosion tests

KCl (Alfa Aesar, >99%), NaCl (Alfa Aesar, >99%) and anhydrous MgCl_2 (Magnesia, >99%, technical grade) were used to synthesize the salt mixture of $\text{MgCl}_2/\text{NaCl}/\text{KCl}$ (60/20/20 mole%). In this work, ~1–2% H_2O (measured by Karl-Fischer titration) was hydrated in the anhydrous MgCl_2 salt due to its strong hygroscopicity, when the salts were exposed in air e.g., during synthesizing the salt mixture. Figure 11 shows a schematic of the experimental set-up used for immersion tests in molten chlorides. In this work, several samples of the C/C-SiC composite were completely immersed in the molten $\text{MgCl}_2/\text{NaCl}/\text{KCl}$ (~150 g) in a high-temperature resistant glassy carbon crucible (HTW Germany, Sigradur® G, GAT 55) with a diameter of ~80 mm and a height of 130 mm. During the experiments, the temperature of the molten salts under argon atmosphere was controlled by a thermocouple close to the molten salt, as shown in Fig. 11. Analogous to previous work,⁹ the heating of the salt mixture was conducted as following: after vacuuming at room temperature ($\leq 30 \text{ mbar}$), the vacuum pump was stopped and the argon gas sweeping started. The salt mixture was heated under argon atmosphere (purity $\geq 99.9999\%$, $\text{H}_2\text{O} \leq 3 \text{ ppm}$ and $\text{O}_2 \leq 2 \text{ ppm}$, 20 l/h (STP), the absolute pressure above the salts was

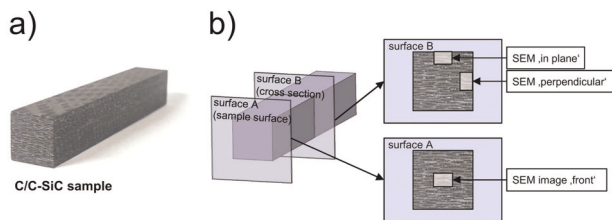


Fig. 12 Overview of different surfaces for the microstructure analysis of the C/C–SiC coupon before and after exposure in molten chloride salt: **(a)** C/C–SiC sample; **(b)** surface A is the front of the coupon, which has direct contact with molten chlorides and surface B is the cross section for “in plane” and “perpendicular” SEM analysis.

~1.1 bar) from room temperature to 200 °C with a heating rate of ~5 K/min, then kept at 200 °C for 1 h to remove residual water in the hygroscopic MgCl₂ salt. After that, it was heated to 700 °C and kept at this temperature for corrosion tests with the immersed coupons of the C/C–SiC composite. The measurements of titration and cyclic voltammetry (CV), which are described in previous work,¹⁹ show that the concentration of the corrosive impurity MgOH⁺ in the salts after the heating process was ~2000 ppm (5×10^{-2} mol/kg(salt)) at 700 °C, while the impurity O²⁻ cannot be detected by CV due to its low solubility in molten chloride salts at 700 °C (~80 ppm in weight).¹⁹ After 500 h exposure at 700 °C, the furnace was cooled down to room temperature under argon atmosphere. The corrosion resistance of the C/C–SiC specimens was analyzed subsequently via different mechanical tests and microstructural analysis.

Mechanical tests

The mechanical properties of the coupons in unexposed state and after exposure in the molten chloride salt were determined and evaluated using compression-shear and –3PB testing. All the experiments were performed up to failure of sample on a universal testing machine (Zwick 1494) at a controlled cross head speed of 1 mm/min at room temperature. The failure stress was calculated from the maximum load. For statistical confirmation three samples per series were tested.

In order to determine the interlaminar shear strength (ILSS_C), compression-shear test was performed according to DIN-EN 658-4²⁰ with a notch distance of 8 mm. The bending properties of the C/C–SiC materials, i.e., 3PB-strength (σ_{3PB}), Young’s modulus (E) and strain of failure (ϵ_{3PB}), were determined by 3PB testing according to DIN-EN 658-3 with a span-to-thickness ratio L/t of 20.²¹ The longitudinal strains were measured with strain gauges on the tensile site of bending specimens. Table 4 gives the configuration overview of the performed mechanical tests and the test dimension, as well as the tested mechanical properties.

Microstructural analysis

In order to analyze the microstructures of the C/C–SiC samples before and after the salt exposure, SEM and EDX spectroscopy were used. Two different perspectives of the samples were analyzed (see Fig. 12): surface A is the front of the C/C–SiC sample; surface B is the cross section of the C/C–SiC samples at a depth of approximately 4 mm to the surface A. Both sample stacks (exposed/non-exposed) originate from the same source material with uniform material composition. As a consequence, we believe that the analysis on the “non-exposed” samples reflects the initial state of the samples before exposure. The analysis of microstructure of surface B was performed on two different areas: horizontal to the fabric layers (in plane) and vertical to the layers (perpendicular). For the analysis a scanning electron microscope (type Gemini Ultra Plus from Zeiss) was used. For the imaging an AsB detector (Auto selective Backscatter) was used and a high voltage of 15 kV was applied. The connected EDX has an X-Max detector from Oxford instruments. The EDX scanning was carried out at the same voltage as the imaging and 30 frames per elemental image were recorded.

DATA AVAILABILITY

The datasets generated during and/or analyzed during the current study are available from the corresponding author on reasonable request.

Received: 12 April 2019; Accepted: 22 November 2019;
Published online: 19 December 2019

REFERENCES

- Renewables 2016: *Renewable Energy Policy Network for the 21st Century Global status Report* (2016).
- Tian, Y. & Zhao, C. Y. A review of solar collectors and thermal energy storage in solar thermal applications. *Appl. Energy* **104**, 538–553 (2013).
- Kruizenga, A. M. *Corrosion Mechanisms in Chloride and Carbonate Salts* (SANDIA Report, 2012).
- Mehos, M. et al. *Concentrating Solar Power Gen3 Demonstration Roadmap* (National Renewable Energy Laboratory, Golden, CO, 2017).
- Vignarooban, K. et al. Vapor pressure and corrosivity of ternary metal-chloride molten-salt based heat transfer fluids for use in concentrating solar power systems. *Appl. Energy* **159**, 206–213 (2015).
- Gomez-Vidal, J. C., Fernandez, A. G., Tirawat, R., Turchi, C. & Huddleston, W. Corrosion resistance of alumina-forming alloys against molten chlorides for energy production. I: Pre-oxidation treatment and isothermal corrosion tests. *Sol. Energy Mater. Sol. Cells* **166**, 222–233 (2017).
- Liu, B., Wei, X., Wang, W., Lu, J. & Ding, J. Corrosion behavior of Ni-based alloys in molten NaCl–CaCl₂–MgCl₂ eutectic salt for concentrating solar power. *Sol. Energy Mater. Sol. Cells* **170**, 77–86 (2017).
- Gomez-Vidal, J. C. & Tirawat, R. Corrosion of alloys in a chloride molten salt (NaCl–LiCl) for solar thermal technologies. *Sol. Energy Mater. Sol. Cells* **157**, 234–244 (2016).
- Ding, W. et al. Hot corrosion behavior of commercial alloys in thermal energy storage material of molten MgCl₂/KCl/NaCl under inert atmosphere. *Sol. Energy Mater. Sol. Cells* **184**, 22–30 (2018).
- Vignarooban, K., Xu, X., Arvay, A., Hsu, K. & Kannan, A. M. Heat transfer fluids for concentrating solar power systems—a review. *Appl. Energy* **146**, 383–396 (2015).
- Andreades, C. et al. *Technical Description of the “Mark 1” Pebble-Bed Fluoride-Salt-Cooled High-Temperature Reactor (PB-FHR) Power Plant*. 153 (Department of Nuclear Engineering, University of California Berkeley, 2014).
- Ding, W. et al. Molten chloride salts for next generation concentrated solar power plants: Mitigation strategies against corrosion of structural materials. *Sol. Energy Mater. Sol. Cells* **193**, 298–313 (2019).
- Peterson, P. F., Forsberg, C. W. & Pickard, P. S. in *Second Information Exchange Meeting on Nuclear Production of Hydrogen* (Argonne National Laboratory, Illinois, USA, 2003).
- Sabharwall, P. et al. *Molten Salts for High Temperature Reactors: University of Wisconsin Molten Salt Corrosion and Flow Loop Experiments—Issues Identified and Path Forward*. (Idaho National Laboratory, Idaho Falls, 2010).
- Heidenreich, B. et al. in *Ceramic Materials and Components for Energy and Environmental Applications*. (eds Jiang, D., Zeng, Y., Singh, M. & Heinrich J.) (Wiley, 2010).
- W. Krenkel. *Development of a Cost Efficient Process for the Manufacture of CMC Components*. *Doctoral Thesis* University of Stuttgart (2000).
- Gern, F. H. & Kochendörfer, R. Liquid silicon infiltration: description of infiltration dynamics and silicon carbide formation. *Compos. Part A: Appl. Sci. Manuf.* **28**, 355–364 (1997).
- Vidal, J. C. & Klammer, N. in *SolarPACES 2018: International Conference on Concentrating Solar Power and Chemical Energy Systems*. (ed Richter, C.) 080006 (AIP Publishing).
- Ding, W., Bonk, A., Gussone, J. & Bauer, T. Electrochemical measurement of corrosive impurities in molten chlorides for thermal energy storage. *J. Energy Storage* **15**, 408–414 (2018).
- DIN EN 658-4: Advanced technical ceramics—mechanical properties of ceramic composites at room temperature—part 4: Determination of interlaminar shear strength by compression loading of notched test specimens (2003).
- DIN EN 658-3: Advanced technical ceramics—mechanical properties of ceramic composites at room temperature—part 3: Determination of flexural strength (2003).
- Bauer, T. et al. in *Molten Salts Chemistry* 415–438. <https://doi.org/10.1016/b978-0-12-398538-5.00020-2> (2013).
- Li, Y. et al. Survey and evaluation of equations for thermophysical properties of binary/ternary eutectic salts from NaCl, KCl, MgCl₂, CaCl₂, ZnCl₂ for heat transfer and thermal storage fluids in CSP. *Sol. Energy* **152**, 57–79 (2017).

ACKNOWLEDGEMENTS

This research has been performed within the DLR-DAAD fellowship program, which is funded by German Academic Exchange Service (DAAD) and German Aerospace

Center (DLR). The authors would like to thank Markus Braun at the DLR-Institute of Engineering Thermodynamics and Daniel Cepeli at the DLR-Institute of Structures and Design for their technical support.

AUTHOR CONTRIBUTIONS

W.D. and Y.S. designed research; W.D., Y.S., and F.K. performed research. All authors analyzed data and contributed to writing the paper.

COMPETING INTERESTS

The authors declare no competing interests.

ADDITIONAL INFORMATION

Correspondence and requests for materials should be addressed to Y.S.

Reprints and permission information is available at <http://www.nature.com/reprints>

Publisher's note Springer Nature remains neutral with regard to jurisdictional claims in published maps and institutional affiliations.



Open Access This article is licensed under a Creative Commons Attribution 4.0 International License, which permits use, sharing, adaptation, distribution and reproduction in any medium or format, as long as you give appropriate credit to the original author(s) and the source, provide a link to the Creative Commons license, and indicate if changes were made. The images or other third party material in this article are included in the article's Creative Commons license, unless indicated otherwise in a credit line to the material. If material is not included in the article's Creative Commons license and your intended use is not permitted by statutory regulation or exceeds the permitted use, you will need to obtain permission directly from the copyright holder. To view a copy of this license, visit <http://creativecommons.org/licenses/by/4.0/>.

© The Author(s) 2019